Corrosion Science 232 (2024) 112043

Contents lists available at ScienceDirect

Corrosion Science

journal homepage: www.elsevier.com/locate/corsci

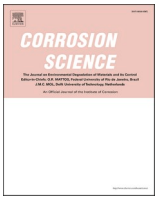

Mechanism of local hydrogen entry into Fe sheets induced by atmospheric corrosion: Significance of potential, pH, and rust layer thickness

Hiroshi Kakinuma [a,*], Sachiko Hiromoto [a,b], Tomohiko Hojo [c], Saya Ajito [a], Motomichi Koyama [a], Eiji Akiyama [a,b]

[a] Institute for Materials Research, Tohoku University, 2-1-1 Katahira, Aoba-ku, Sendai 980-8577, Japan
[b] Research Center for Structural Materials, National Institute for Materials Science, 1-2-1 Sengen, Tsukuba 305-0047, Japan
[c] Faculty of Engineering, Tohoku Gakuin University, 3-1 Shimizukoji, Wakabayashi-ku, Sendai 984-8588, Japan

ARTICLE INFO

Keywords:
Iron
Hydrogen permeation
Atmospheric corrosion

ABSTRACT

Local hydrogen entry under a NaCl droplet on Fe sheets was analysed by employing a hydrogenochromic sensor and electrochemical hydrogen permeation tests. Large crystallographic pits barely promoted hydrogen entry, because crystallographic pitting proceeded at potentials higher than the potential of the hydrogen evolution reaction. Hydrogen entry was accelerated because of acidification under an island-like rust layer. The rust layer became thick in its outer regions, mainly owing to severe corrosion and alkalisation around the rust-formed area. Hydrogen entry was prominent under the thick rust layer after disappearance of the droplet, owing to the high concentrations of chloride ions and protons.

1. Introduction

Hydrogen atoms enter steels owing to corrosion under atmospheric conditions, and the atomic state hydrogen in steels often reduces the ductility of steels; this is known as hydrogen embrittlement [1–4]. In particular, the susceptibility to hydrogen embrittlement tends to increase as the tensile strength of the steel increases. Thus, hydrogen embrittlement limits the use of high-strength steels that have excellent mechanical properties. Developing a technique for prohibiting hydrogen entry is crucial to exploit the potential benefits of high-strength steels, and the detailed mechanism of hydrogen entry under atmospheric conditions must be elucidated to develop such a technique.

Hydrogen entry into steels owing to corrosion in atmospheric environments has been extensively studied over the past few decades [5–9]. Environmental factors, such as the solution pH and potential, and corrosion reactions have been suggested to play important roles [5,8,10–12]; however, the hydrogen entry mechanism is still unclear. The main obstacle is that the detection of corrosion-induced hydrogen entry is challenging because the amount of hydrogen that enters steels owing to corrosion is very small and hydrogen entry occurs locally.

Conventionally, thermal desorption spectroscopy (TDS) [7,11] and electrochemical hydrogen permeation tests with a Devanathan cell [13–15] have been used to analyse the hydrogen entry behaviour due to corrosion. Akiyama *et al.* analysed the diffusible hydrogen content and hydrogen permeation current of pre-rusted specimens and suggested that the growth of the rust layer is responsible for enhancing hydrogen entry [11]. Because TDS and electrochemical hydrogen permeation tests are performed to measure the average amount of hydrogen in a specimen or the average value of the hydrogen flux within an electrode area, specimens corroded under different conditions are used to analyse the macroscale hydrogen entry. Thus, analysing the local hydrogen entry and distribution in steels is difficult. Under corrosion conditions, time-dependent distributions of the solution pH and potential exist on the steel surface in addition to the anodic and cathodic reaction sites, which also change kinetically. Therefore, to elucidate the local hydrogen entry mechanism with respect to the pH, potential, and corrosion reactions, the corrosion and local hydrogen entry behaviour should be simultaneously analysed.

To analyse the time-dependent hydrogen distribution, visualisation techniques for hydrogen in metals have been studied. A thin layer of a metal oxide or Ir complex formed on a metal surface has been used to visualise the hydrogen distribution in the metal [16–18]. A scanning Kelvin probe (SKP), which measures the work function on a metal surface by scanning a probe near the metal surface, has also been utilised to visualise the hydrogen distribution [19]. Although an SKP offers a high spatial resolution for visualising hydrogen entry due to corrosion [9,20,

* Corresponding author.
E-mail address: hiroshi.kakinuma.a1@tohoku.ac.jp (H. Kakinuma).

https://doi.org/10.1016/j.corsci.2024.112043
Received 16 February 2024; Received in revised form 25 March 2024; Accepted 5 April 2024
Available online 9 April 2024

21], real-time visualisation of corrosion-induced hydrogen entry remains challenging.

In our previous study, we developed a hydrogenochromic sensor using polyaniline (PANI) [22] and successfully visualised the hydrogen entry behaviour under a NaCl aqueous solution droplet *in situ* [23]. Under a droplet of 3 wt% NaCl on an Fe sheet, large crystallographic pits were formed during the early stages of corrosion, but hydrogen entry was barely promoted. In contrast, hydrogen entry was clearly enhanced owing to the large spherical pits on an Fe sheet immersed in a bulk 3 wt % NaCl solution [24]. This discrepancy indicates that corrosion-induced hydrogen entry does not necessarily correspond to the amount of dissolved Fe. In addition, local hydrogen entry is known to occur under the rust layer even after the NaCl droplets on the Fe surface disappear [20, 23]. However, the critical factors for local hydrogen entry after the droplet disappearance have not yet been elucidated. To clarify these ambiguous points, in this study, we visualised the hydrogen entry behaviour under a NaCl aqueous solution droplet using the hydrogenochromic sensor and conducted electrochemical hydrogen permeation tests using a Devanathan cell to analyse the hydrogen entry behaviour with respect to the solution pH and potential. Furthermore, we examined the pH distribution in the NaCl droplet using a pH indicator to clarify the role of pH distribution in hydrogen entry and rust precipitation. We also determined the critical role of the rust layer thickness in hydrogen entry after the disappearance of the droplet.

2. Material and methods

2.1. Specimen

An Fe sheet (99.5%) with a thickness of 0.5 mm was used as the specimen. The specimen was annealed in a salt bath at 1173 K for 900 s and cut to achieve a size of 30 mm × 30 mm. Electrical polishing was conducted in a mixed solution of perchloric acid (60mass%, 210 mL) and acetic acid (99.7mass%, 790 mL) via polarisation at a constant voltage of 50 V. After being polished, the specimen surface was rinsed with distilled water and dried with N_2 gas.

Ni plating was conducted on one side of the specimen in a solution containing $NiSO_4$ $6H_2O$ (250 g L^{-1}), $NiCl_2$ $6H_2O$ (45 g L^{-1}), and H_3BO_3 (40 g L^{-1}) at 333 K via galvanostatic polarisation of –30 A m^{-2} for 180 s. A Pt wire was used as a counter electrode. After Ni plating was performed, the specimen was rinsed with water and dried with N_2 gas. The estimated thickness of the Ni layer was approximately 400 nm [22]. The Ni layer was utilised to improve the hydrogenochromic properties of the PANI layer [22]. On the Ni layer, a PANI layer was electrochemically polymerised in a 0.5 M H_2SO_4-0.5 M aniline solution at a constant voltage of 1 V for 200 s. A Pt wire was used as a counter electrode. The specimen was rinsed with water and dried with N_2 gas after polarisation. The bare surface on the other side was polished using a SiC paper (#1500). The final thickness of the specimen was *ca.* 0.4 mm. After being polymerised and polished, the specimen was stored in ambient air for 24 h prior to the hydrogen visualisation tests.

2.2. Hydrogen visualisation tests

Fig. 1a shows the experimental setup for the hydrogen visualisation test. In this study, the surface covered with the PANI layer is referred to as the PANI side, and the other surface is the bare Fe side. The specimen was set in an acrylic cell, and the droplet (150 μL) of a 0.1 M NaCl aqueous solution or a 0.1 M NaCl-50 mM thymol blue aqueous solution was placed on the bare Fe side. Thymol blue was used to visualise the pH distribution inside the NaCl droplet. Immediately after the NaCl solution was dropped, optical images of the bare Fe side were captured every 300 s using LED lamps and a digital camera. The interval between the dropping and the first shooting was less than 60 s; thus, the time when the first optical image was captured was defined as 0 h. The humidity and temperature inside the acrylic cell were measured using a hygro-

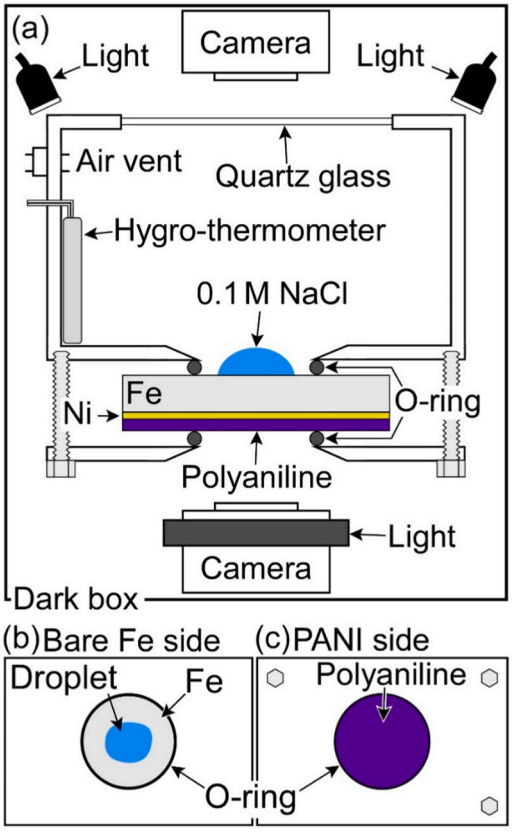

Fig. 1. (a) Experimental setup for hydrogen visualisation test. Schematic diagrams of (b) the bare Fe and (c) PANI sides.

thermometer. The temperature remained almost constant at approximately 298 K during the tests. Figs. 1b and 1c are schematic diagrams of the bare Fe and PANI sides, respectively. The NaCl droplet was placed on the bare Fe side without contact with the O-ring. The purple area inside the O-ring of the PANI side was the PANI layer, and optical images of the PANI side were captured every 300 s using a digital camera and halogen lamp for 24 h. All the images were captured in a dark box.

2.3. Electrochemical hydrogen permeation tests

To measure the hydrogen permeation current densities of the specimen immersed in the NaCl solution at pH 4.0, 3.0, 2.0, and 1.0 (adjustment with HCl), electrochemical hydrogen permeation tests were conducted using the Devanathan cell [13]. After electrical polishing, Ni plating was conducted on one side of the specimen by employing the procedure described in Section 2.1. The other side of the specimen was mechanically ground using the SiC paper (#1500). The final thickness of the specimen was *ca.* 0.4 mm. The Ni-plated surface was polarised at a constant potential of 0.1 V vs. Hg/HgO (1 M NaOH) in 1 M NaOH for 24 h to measure the background current. Subsequently, the other side (hydrogen entry side, hereafter) of the specimen was immersed in 0.1 M or 1 M NaCl at pH values of 4.0, 3.0, 2.0, and 1.0 for 24 h, and the hydrogen permeation current was measured on the Ni-plated surface. The open-circuit potentials (OCPs) of the hydrogen entry side were measured using a Ag/AgCl (3.33 M KCl) reference electrode.

2.4. Surface characterisation

After hydrogen visualisation tests and electrochemical hydrogen permeation tests, surface analyses were conducted using an optical microscope and a micro-focused X-ray fluorescence spectrometer (μ-XRF). Quantitative point analyses of the Cl concentration were conducted

using μ-XRF under vacuum at an accelerating voltage of 15 V and an irradiation current of *ca.* 0.3 mA. A Rh tube was utilised as the X-ray source, and the spot size was 100 μm. To observe the corrosion morphology under the rust layer, rust was removed by immersing the specimen in a diammonium hydrogen citrate solution (200 g L^{-1}) for approximately 500 s at 333 K. To measure the surface roughness of the specimen, the hydrogen entry side was analysed using a one-shot 3D measuring microscope before and after rust removal.

3. Results and discussion

3.1. Corrosion morphology and hydrogen entry under a NaCl droplet on an Fe sheet

Fig. 2a presents the optical image of the bare Fe side after the hydrogen visualisation test. The black dashed circle indicates the edge of the droplet on the Fe surface (droplet edge, hereafter) before droplet disappearance. As shown in Fig. 3, the droplet diameter increased until 7 h. Fig. 2a indicates the maximum droplet edge size. As shown in Fig. 2a, a brown rust layer was formed under the droplet. Fig. 2b displays an optical image of the bare Fe side after rust removal. The Fe surface under the rust layer lost its metallic lustre. Fig. 2c shows the optical image of the PANI side after the hydrogen visualisation test. The white dashed circle indicates the droplet edge on the bare Fe side. The optical image depicted in Fig. 2c was flipped horizontally to synchronise the positions of the images in Figs. 2a, 2b, and 2c. As shown in Fig. 2c, the colour of the PANI layer partially changed from purple to light blue. Because the PANI layer is brightened owing to the reaction with atomic state hydrogen [22,24], the colour change indicates hydrogen entry. The colour-changed area on the PANI side corresponded to the corroded area on the bare Fe side.

Figs. 2d and 2e show optical micrographs of the areas with and without metallic lustre, respectively, which are indicated by the blue arrows in Fig. 2b. In the area with metallic lustre (Fig. 2d), corrosion was not confirmed, whereas the area without metallic lustre was corroded and black dots were observed (Fig. 2e). Therefore, the promotion of hydrogen entry was confirmed in the corroded area of the Fe surface. In addition to the general corrosion shown in Fig. 2e, large crystallographic pits (Fig. 2f) were observed in the area indicated by the orange arrow in Fig. 2b. However, no prominent colour change occurred in the PANI layer around the crystallographic pits compared with the other corroded areas. This suggests that the amount of dissolved Fe is not a critical factor for hydrogen entry under a droplet of NaCl. Rather, hydrogen entry seems to depend on the pH and potential on the Fe surface, which changes continuously during the corrosion process under atmospheric conditions [5,6,25].

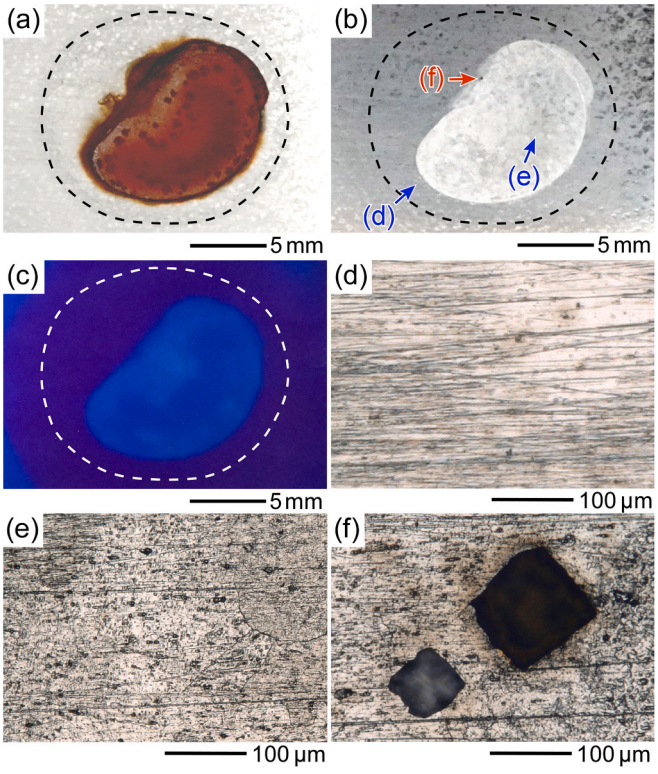

Fig. 2. Optical images of the hydrogen entry side after hydrogen visualisation test (a) before and (b) after rust removal. (c) Optical image of the PANI side after hydrogen visualisation test. (d), (e), (f) Optical micrographs of the areas indicated by the blue and orange arrows in (b).

The upper and lower rows of the optical images in Fig. 3 show the bare Fe and PANI sides, respectively, during the hydrogen visualisation test. After 2 h, corrosion started in the area indicated by the red arrow, and brown rust precipitates were formed. The initiation site of corrosion corresponded to the area where the crystallographic pits shown in Fig. 2f were observed. At 3 h, the droplet and rust layer spread, but no colour change was observed on the PANI side, indicating less hydrogen entry than the detection level. After 5 h, the colour of the PANI layer changed from purple to blue and became brighter with time. After 13 h, the droplet was barely visible owing to drying. After the disappearance of the droplet, almost no significant colour change was observed on the bare Fe and PANI sides. The optical images shown in Fig. 3 were converted to a video file (see Supplemental Video 1). To confirm the reproducibility of these results, the same experiment was conducted on another specimen (see Supplemental Video 2).

To analyse the corrosion process and hydrogen entry in detail, the colour of the PANI layer was quantitatively evaluated by performing image analysis. The *R* (red), *G* (green), and *B* (blue) values of each pixel in the optical image of the PANI side presented in Fig. 3 were extracted, and the hue, *H*, was calculated using the following formula [26]:

$$H = 0,\ (R = G = B) \tag{1}$$

$$H = 60 \times (G - B) / (I_{max} - I_{min}),\ (I_{max} = R) \tag{2}$$

$$H = 60 \times (B - R) / (I_{max} - I_{min}) + 120,\ (I_{max} = G) \tag{3}$$

$$H = 60 \times (R - G) / (I_{max} - I_{min}) + 240,\ (I_{max} = B) \tag{4}$$

where I_{max} and I_{min} represent the maximum and minimum values among the *R*, *G*, and *B* values, respectively. Furthermore, the difference in hue, ΔH, was calculated using the following formula:

$$\Delta H = H_0 - H_t \tag{5}$$

where H_0 and H_t denote the values of *H* at 0 h and time *t*, respectively. Similar to the ΔY value [22–24,27,28], the ΔH value of the PANI layer has been confirmed to roughly correspond to the integrated value of the hydrogen flux (see Supplemental Figs. 1 and 2). Fig. 4 shows the contour maps of ΔH of the PANI side obtained from the images in Fig. 3. As revealed in Fig. 4a, ΔH started to increase after 4 h, but no increase in ΔH was observed around the initiation site of the crystallographic pits indicated by the white arrow. Thus, the crystallographic pits, which occurred during the initial stage of corrosion under a droplet of NaCl, barely promoted hydrogen entry. However, hydrogen entry was observed beneath the rust deposits in the form of an island that appeared after the pit initiation in the earlier stage. The maximum ΔH value was confirmed near the droplet edge (white dashed curve) after 11 h. Because the droplet is thinner near the droplet edge than at the centre, O_2 was thought to be readily supplied from the air, promoting corrosion and corrosion-induced hydrogen entry.

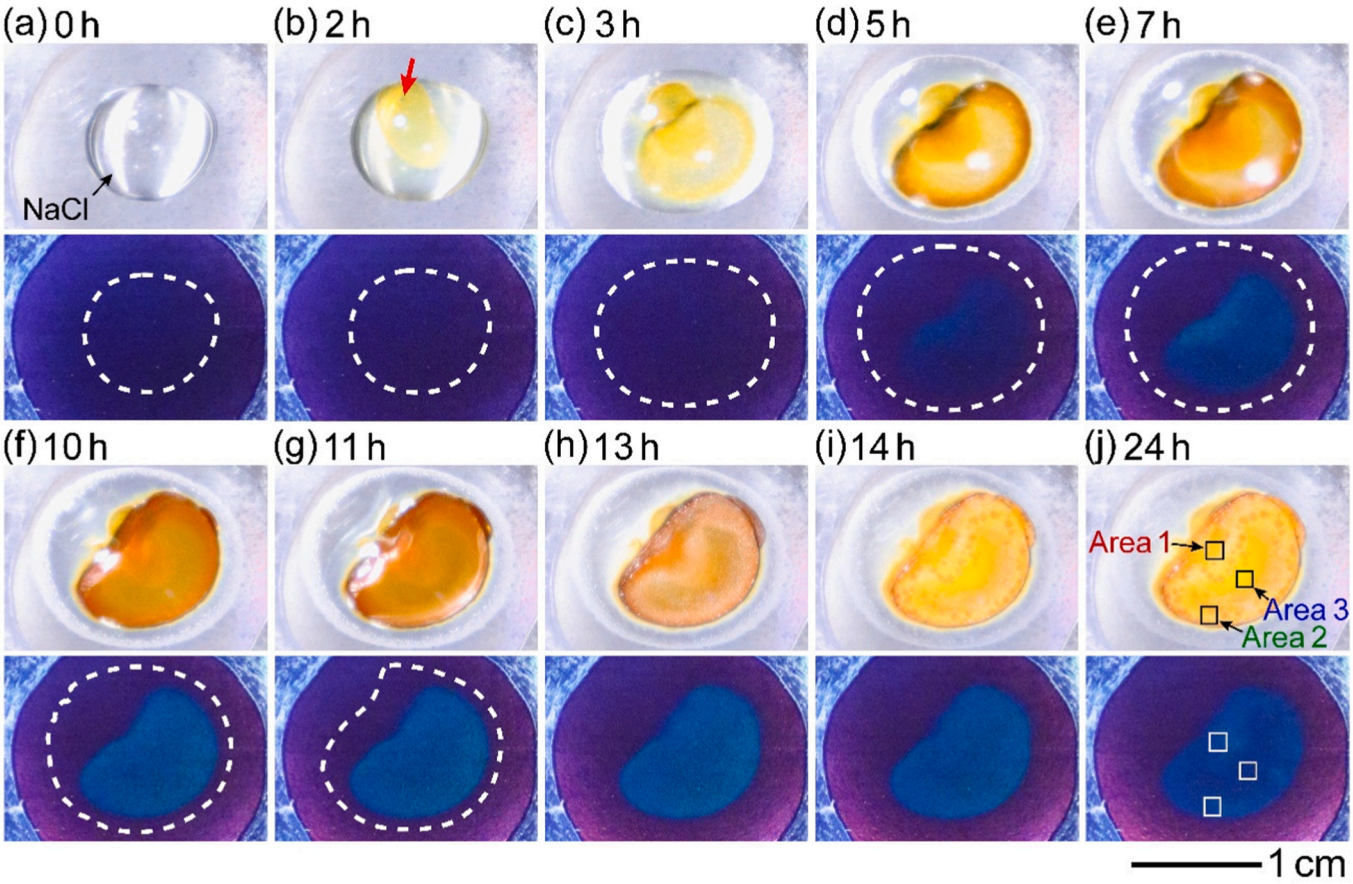

Fig. 3. Optical images of the bare Fe and PANI sides during the hydrogen visualisation test. The red arrow indicates the initiation site of the crystallographic pits shown in Fig. 2f.

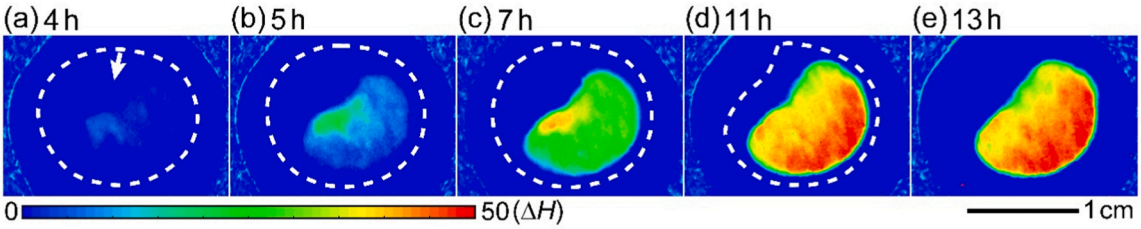

Fig. 4. Contour map of ΔH of the PANI side shown in Fig. 3. The white arrow in (a) indicates the initiation site of the crystallographic pits shown in Fig. 2f.

3.2. Relationship between the morphology of the droplet, corrosion processes, and hydrogen entry

Based on the results obtained thus far, it can be suggested that the growth of the rust layer and morphology of the droplet play important roles in hydrogen entry. The area of the rust layer and area inside the droplet edge (indicated by the white dashed circle in Fig. 3) were calculated by performing image analysis based on the optical images in Fig. 3, and the values normalised by the respective maximum values are defined as A_{rust} and A_{drop}, respectively. The orange and blue curves in Fig. 5a indicate A_{rust} and A_{drop}. Both A_{rust} and A_{drop} slowly increased for 2 h. In this study, the initiation period, during which corrosion gradually proceeded until 2 h, is referred to as the 1st stage. After 2 h, the values of A_{rust} and A_{drop} considerably increased. The increase in A_{drop} caused the thinning of the droplet and an increase in the cathodic area, promoting the oxygen reduction reaction (ORR). Consequently, the corrosion and growth of the rust layer were promoted as A_{drop} increases. The period during which A_{rust} and A_{drop} rapidly increased until the disappearance of the droplet is referred to as 2nd stage. The period when the droplet was barely observed is referred to as 'after disappearance of the droplet'. The time variation of relative humidity measured by the hydro-thermometer indicated in Fig. 1 is also shown as a reference. Because the relative humidity in the acrylic cell was approximately 45%RH after disappearance of the droplet, it is thought that the rust layer did not completely dry out. Fig. 5b shows the time variations of the average ΔH values in Areas 1–3 of the PANI side, as indicated by the black and white rectangles in Fig. 3j. In the 1st stage, the increase in ΔH was not confirmed. After 4 h, the ΔH in Areas 1 and 3 started to increase, followed by the increase in the ΔH in Area 2. It was confirmed that the corrosion-induced hydrogen entry barely occurred in the 1st stage, while the hydrogen entry was clearly enhanced in the 2nd stage with the rapid corrosion.

At 7 h, the ΔH in Area 1 reached 40 and remained constant until the droplet disappears. In Areas 2 and 3, which were close to the droplet edge, ΔH continued to increase until the droplet disappears. Area 1 was close to the pits initiated during the 1st stage, which presumably

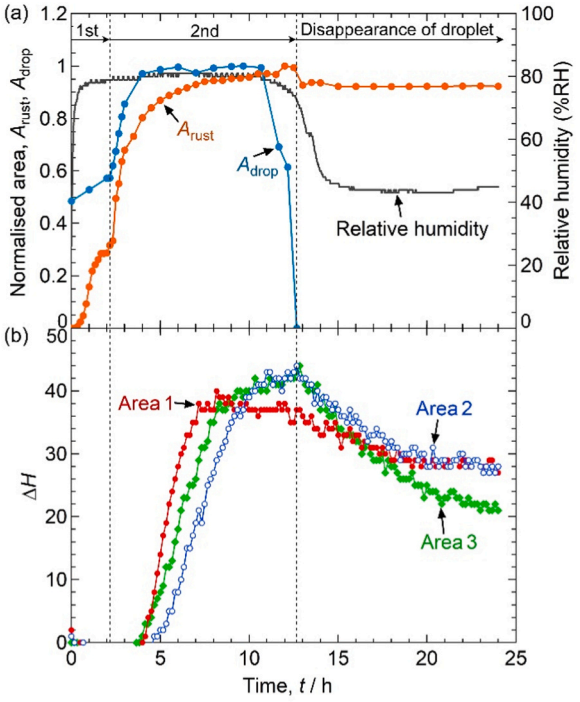

Fig. 5. (a) Time variations of the normalised areas of the rust layer (A_{rust}), inside the droplet edge (A_{drop}), and relative humidity during the hydrogen visualisation test shown in Fig. 3. (b) Time variations of the average ΔH value of Areas 1–3 of the PANI side indicated by the black and white rectangles shown in Fig. 3j.

triggered subsequent corrosion in the island-like rust region. Thus, up to 6 h, the order of ΔH in all the areas was as follows: Area 1 > Area 2 > Area 3. As corrosion proceeded, corrosion and hydrogen entry were promoted in Areas 2 and 3 more than in Area 1 after 9 h, because Areas 2 and 3 were close to the droplet edge where the droplet is thin. Under the thin droplet, the corrosion rate increases [29], because the ORR is accelerated [30,31]. Therefore, it can be estimated that the decrease in the potential and pH due to severe corrosion under the rust-formed area enhanced hydrogen entry near the droplet edge, where the ORR is promoted.

3.3. Roles of pH and potential in corrosion-induced hydrogen entry under NaCl droplet

The solution pH and potential on a metal surface are important factors for hydrogen entry [5,8,23,24,32]. The foregoing results suggested that the pH and potential decreased in the corroded area of the Fe surface under the NaCl droplet, accelerating hydrogen entry. Subsequently, electrochemical hydrogen permeation tests were conducted to determine the critical pH and potential that drastically enhance hydrogen entry. The hydrogen permeation current density was measured using the Devanathan cell. For the hydrogen entry side, 0.1 M NaCl at pH 4.0, 3.0, 2.0, and 1.0 were used, and this side of the specimen was immersed in the pH-adjusted NaCl solution. Fig. 6a and b show the OCPs of the hydrogen entry side in different NaCl solutions and the hydrogen permeation current densities of the hydrogen detection side, respectively. As a reference, the results for 1 M NaCl (pH 4.0) are also shown. In 0.1 M NaCl, the OCP was –0.2 V at pH 4.0, while it decreased to –0.65 V at pH 3.0. Notably, the OCP at pH 2.0 was approximately 0.1 V higher than that at pH 3.0. As shown in Fig. 6b, almost no hydrogen permeation current was detected at pH 4.0, regardless of the chloride ion concentration. However, a hydrogen permeation current was detected at both pH 3.0 and 2.0, and the hydrogen permeation current at pH 2.0 was larger than that at pH 3.0.

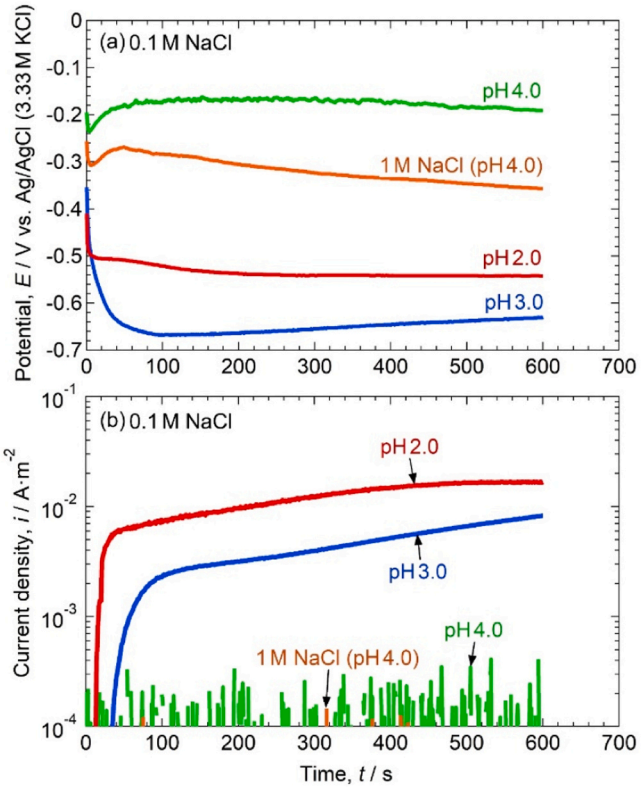

Fig. 6. (a) Time variations of the OCPs of the hydrogen entry side and (b) current density of the hydrogen detection side during the hydrogen permeation tests. For a solution at hydrogen entry side, 0.1 M NaCl at different pH values and 1 M NaCl at pH 4 were used.

Fig. 7 displays the optical micrographs of the hydrogen entry side after the hydrogen permeation test shown in Fig. 6. No corrosion was observed after immersion in 0.1 M NaCl (pH 4.0), whereas corrosion proceeded in 0.1 M NaCl at pH 3.0 and 2.0 (see Supplemental Fig. 3 for the optical image of the whole electrode areas). At pH 2.0, black dots, which were also observed in Fig. 2e, were confirmed. Figs. 6 and 7 indicate that hydrogen entry was not promoted at pH 4.0 owing to the non-corroded Fe surface and that lower pH results in more severe corrosion, thus accelerating hydrogen entry. Only in 1 M NaCl (pH 4.0), eight crystallographic pits larger than 10 μm and many small

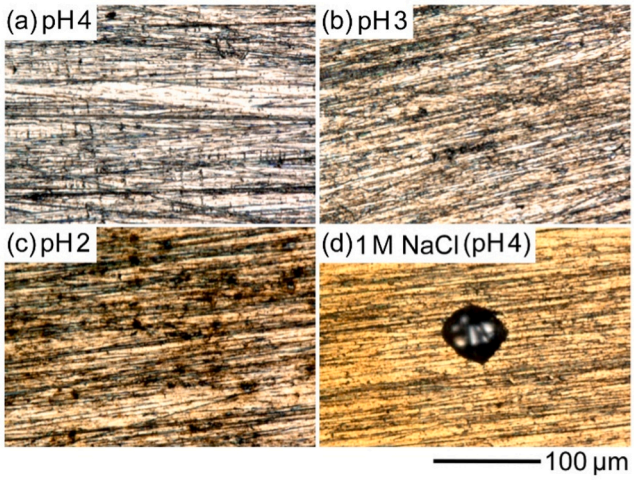

Fig. 7. Optical micrographs of the hydrogen entry side after the hydrogen permeation tests shown in Fig. 6.

crystallographic pits were formed. The corrosion morphology was similar to that of the crystallographic pits formed during the initial stage of corrosion under the NaCl droplet (Fig. 2f). It was concluded that the crystallographic pits are initiated in a weakly acidic NaCl solution and that the potential when the crystallographic pits form is higher than that when general corrosion proceeded in 0.1 M NaCl at pH 3.0 and 2.0.

Fig. 8 depicts the *E*-pH diagram of Fe. The red dots and green rectangle indicate the OCPs of the specimen immersed in 0.1 M NaCl (pH 4.0, 3.0, and 2.0) or 1 M NaCl (pH 4.0) for 600 s, as shown in Fig. 6, respectively. The results of 0.1 M NaCl (pH 1.0) are also shown as a reference. At pH 4.0, the OCP was higher than the electrode potential of the hydrogen evolution reaction (HER) indicated by the dashed blue line, regardless of the chloride ion concentration. It was concluded that the hydrogen entry was barely enhanced by the initiation of large crystallographic pits in 1 M NaCl at pH 4.0, because crystallographic pitting proceeds at potentials higher than the electrode potential of the HER at pH 4.0. In contrast, the OCP was lower than the electrode potential of the HER at pH 3.0, 2.0, and 1.0. Furthermore, below pH 3.0, the OCP increased with the decrease in pH. The red line was plotted by using the least-squares method based on the OCPs at pH 3.0, 2.0, and 1.0, and the slope was –62 mV pH^{-1}, which is close to the slope of the HER (–59 mV pH^{-1}). The increase in the OCP below pH 3.0 is suggested to be caused by the increase in the electrode potential of the HER. As shown in Fig. 6b, the hydrogen permeation current densities increased with a decreasing pH, indicating that the increase in the coverage of the adsorbed hydrogen on the Fe surface, which increased because of the decrease in pH, mainly contributed to the acceleration of hydrogen entry on the corroded area of the Fe surface.

These results suggested that a pH distribution exists inside the droplet and plays a critical role in hydrogen entry. Hydrogen entry was clearly shown to be accelerated owing to acidification lower than pH 4.0 on the corroded area. However, hydrogen entry was not detected in the non-corroded area, as shown in Figs. 2 and 3. The ORR is likely to occur as the main cathodic reaction on the non-corroded area of the Fe surface in a neutral or alkaline NaCl solutions. Thus, it can be estimated that the alkalisation of the non-corroded area occurred owing to the ORR, resulting in almost no hydrogen entry.

The hydrogen entry behaviour and pH distribution in the NaCl droplet were simultaneously visualised by using the PANI layer and the 0.1 M NaCl-50 mM thymol blue solution. Thymol blue is a pH indicator;

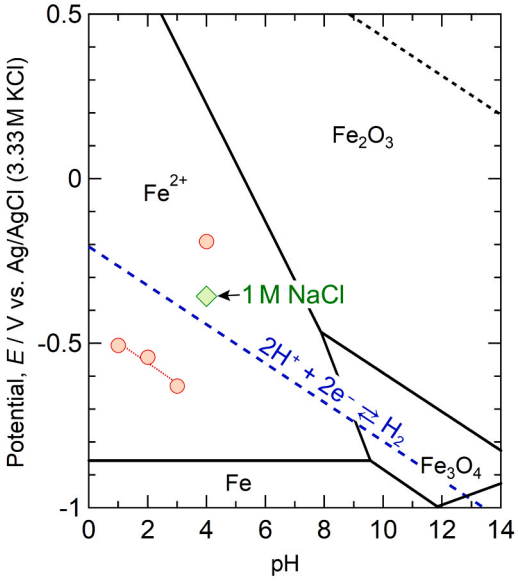

Fig. 8. *E*-pH diagram of Fe. The red dots and green rectangle indicate the OCP of the Fe sheet in 0.1 M NaCl at each pH and 1 M NaCl at pH 4.0, respectively, shown in Fig. 6. The OCP in 0.1 M NaCl at pH 1.0 is shown as a reference.

the colour changes from orange or yellow to blue owing to a pH change from near-neutral or weakly acidic to alkaline [33]. As shown in Fig. 9a, the colour of the droplet was yellow at 0 h, because the pH of the solution was *ca.* 5.5. At 1.1 h, a large pit was initiated in the area indicated by the red arrow and the solution pH remained weakly acidic or near-neutral. At 1.5 h, yellow and blue areas appeared in the droplet, indicating that the solution pH near the corroded area was neutral or weakly acidic, whereas alkalisation occurred in the non-corroded area owing to the ORR. At 3 h, the corroded area spread rapidly (2nd stage), but the pH on the corroded area remained neutral or weakly acidic, barely enhancing hydrogen entry. The initiation site of the large pit was also alkaline at 3 h, implying that the pit growth stopped and the ORR proceeded. After 6 h, the colour of the PANI layer started to change in areas corresponding to the corroded area on the bare Fe side. However, no hydrogen entry was observed in the non-corroded area. This result confirmed that hydrogen entry is not promoted in the non-corroded area, because the solution pH and potential are high owing to the ORR. Because hydrogen entry was confirmed under the rust layer as the colour of the rust layer became dark, local acidification is suggested to occur under the rust layer because of the hydrolysis reaction of Fe ions [32]. The optical images shown in Fig. 9 were converted to a video file (see Supplemental Video 3).

3.4. Hydrogen entry behaviour under rust layer after disappearance of droplet

As shown in Fig. 5b, ΔH gradually decreased in Areas 1−3 after the disappearance of the droplet; ΔH remained at 28 in Areas 1 and 2 but continuously decreased in Area 3. The decrease in the ΔH value indicates that hydrogen entry ceased, because the colour of the PANI layer returned to the original colour very slowly [22]. Fig. 10a presents the contour map of ΔH of the PANI layer at 24 h, as shown in Fig. 3j. The optical image of the bare Fe side after rust removal (Fig. 2b) was binarised to emphasise the degree of the colour change due to corrosion (Fig. 10b). As revealed in Fig. 10b, the degree of colour change was small at the centre of the corroded area and relatively large at the outer regions in the corroded area. Figs. 10c and 10d show optical micrographs of the areas indicated by the blue arrows in Fig. 10b. In the area where the degree of colour change was high (Fig. 10c), the specimen surface was severely corroded and small spherical pits with a diameter of 10–50 μm were formed. The surface was slightly etched, visualizing the grain boundaries in the area where the degree of the colour change was low (Fig. 10d). Thus, the density of the red pixels in the binarised image (Fig. 10b) indicates the degree of corrosion. A comparison between Figs. 10a and 10b reveals that ΔH tends to be high in the severely corroded areas. Hydrogen entry was expected to be promoted by the severe corrosion under the rust layer after the disappearance of the droplet, because no such distribution of ΔH existed before the disappearance of the droplet, as shown in Fig. 4e.

The thick rust layer is likely to contain a large amount of the NaCl solution after the disappearance of the droplet. The degree of corrosion after the disappearance of the droplet possibly depended on the thickness of the rust layer. Fig. 11a presents an optical image of the bare Fe side of another specimen after a hydrogen visualisation test under the same conditions as the experiment shown in Fig. 2. Fig. 11b depicts the surface roughness of the observation area shown in Fig. 11a. In Fig. 11b, the standard height corresponds to the height of the Fe surface where the rust was not formed, meaning that the height indicates the thickness of the rust layer. As shown in Fig. 11b, the thickness of the rust layer increased in the outer regions than in the centre, probably because severe corrosion increased the concentration of Fe ions and the generation of oxyhydroxide and hydroxide of Fe ions [34,35] was promoted by alkalisation around the rust-formed area (Fig. 9). Figs. 11c and 11d reveal the optical image and contour map of ΔH of the PANI side, respectively. The ΔH of the PANI layer was relatively higher in the outer region of the rust layer than in the central region. The thick rust layer is

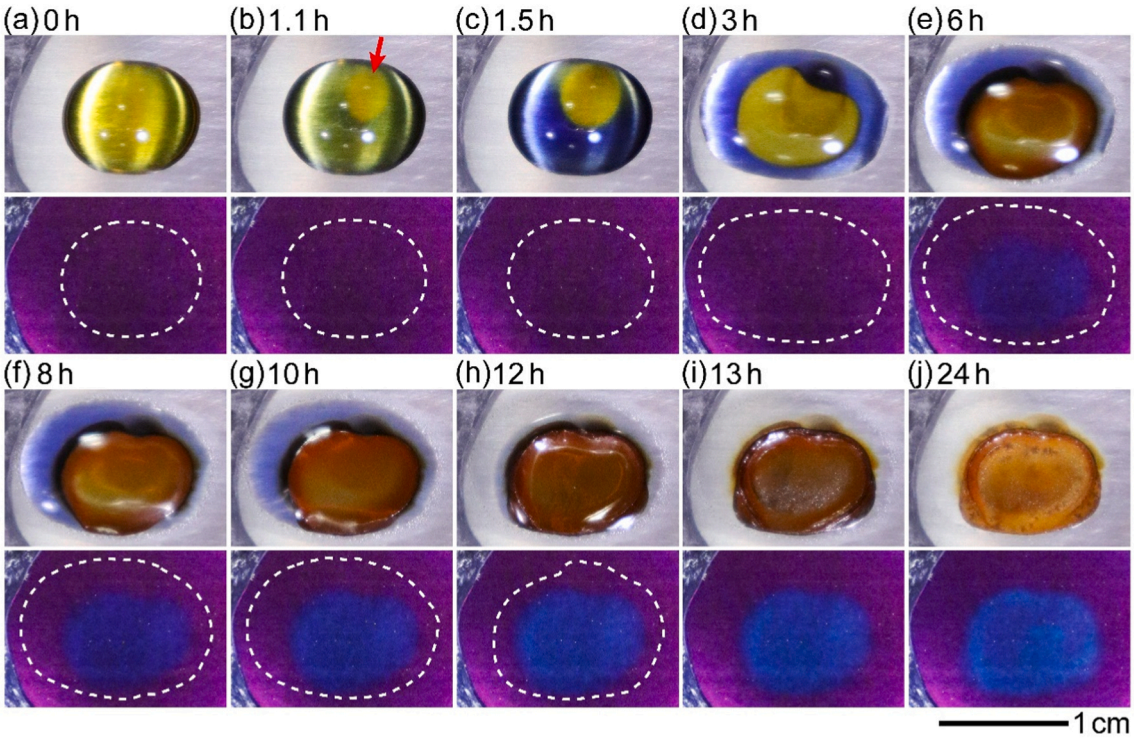

Fig. 9. Optical images of bare Fe and PANI sides during hydrogen visualisation test using the droplet of 0.1 M NaCl-50 mM thymol blue. The red arrow indicates the initiation site of corrosion.

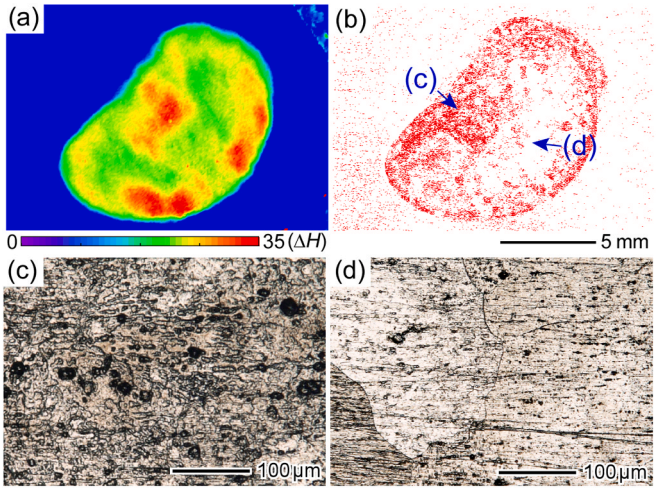

Fig. 10. (a) Contour map of ΔH of the PANI side after 24 h of the hydrogen visualisation test shown in Fig. 3. (b) Binarised image of the optical image shown in Fig. 2b. (c), (d) Optical micrographs of the area indicated by the blue arrows in (b).

considered to contain a large amount of chloride ions; therefore, severe corrosion continuously proceeded with the concentrated NaCl solution for a long time, even after the disappearance of the droplet.

After the hydrogen visualisation test, point analyses of the Cl concentration were performed using μ-XRF. The blue curve in Fig. 11e represents the line profile of ΔH on the line shown by the black line in Fig. 11d. The red rectangles in Fig. 11e denote the Cl concentration in the area indicated by light blue dots A–D in Fig. 11a. Point analyses were conducted at two points in each area, and the average value of the two points is shown as red rectangles in Fig. 11e. The Cl concentration and ΔH value were high at the outer region in the rust layer, indicating that the thick rust layer at the outer region contained a large amount of chloride ions. The high concentration of chloride ions was thought to cause severe corrosion, resulting in the acceleration of hydrogen entry after the disappearance of the droplet.

Consequently, the amount of hydrogen that permeated under the thick rust layer was greater than that under the thin rust layer. Li *et al.* [11] investigated the hydrogen permeation current of Fe sheets (99.5%) pre-rusted under different conditions during the drying process and suggested that the peak of the hydrogen permeation current density in the drying process increased depending on the thickness of the rust layer on the specimens. In the present study, it was clarified that hydrogen entry locally proceeds even under a rust layer on an Fe sheet after the disappearance of the droplet and that the local hydrogen entry continuously proceeds depending on the thickness of the rust layer formed under a small droplet.

3.5. Mechanism of corrosion-induced hydrogen entry into an Fe sheet under a NaCl droplet

Fig. 12 shows a schematic of the mechanism of corrosion-induced hydrogen entry into an Fe sheet under a NaCl droplet, as inferred from the aforementioned experimental results. The time-dependent change in the hydrogen entry behaviour and the effects of the potential, pH, and rust precipitation can be expressed as follows: during the initial stage, the Fe surface is dissolved, forming a large crystallographic pit(s) with the ORR as the main cathodic reaction [8,36].

$$O_2 + 2H_2O + 4e^- \rightarrow 4OH^- \quad (6)$$

Because the ORR is promoted near the droplet edge where O_2 is readily supplied, crystallographic pits tend to be initiated near the droplet edge. As the crystallographic pits are initiated, the pH decreases to *ca.* 4.0 (weakly acidic) around the pits. Because the potential of the pit initiation site is higher than the electrode potential of the HER, and the solution pH is not sufficiently low, hydrogen entry is barely promoted by crystallographic pitting. In addition, the pH locally increases because of the ORR on the non-corroded area without promoting hydrogen entry.

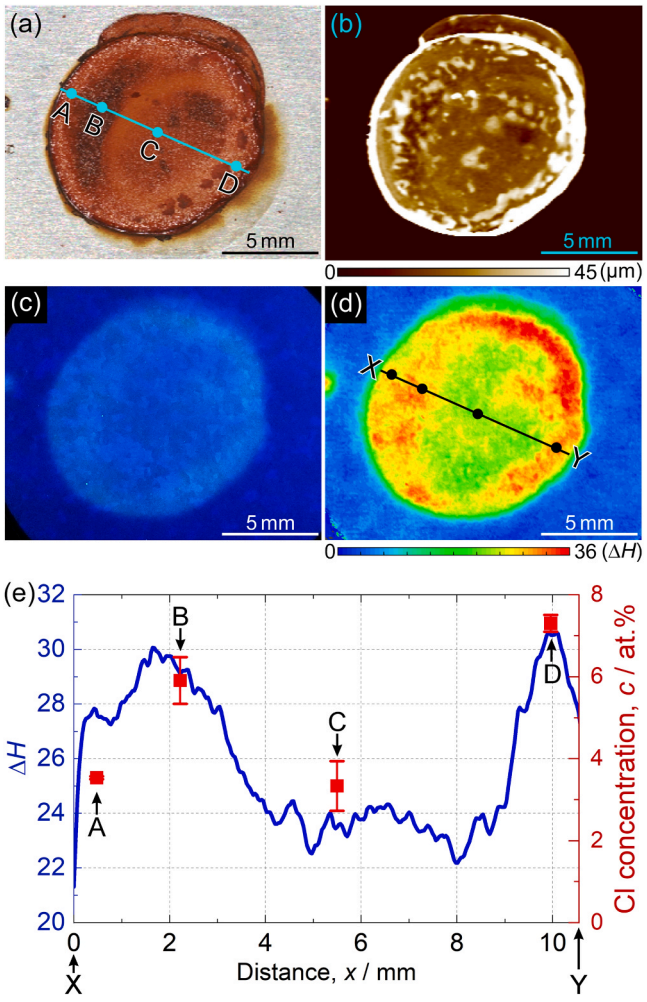

Fig. 11. Optical image of (a) bare Fe and (c) PANI sides. (b) Surface roughness of the bare Fe side. (d) Contour map of ΔH calculated using the image in (c). (e) Line profile of ΔH on the black line in (d) and point analysis of Cl concentration at points A–D in (a).

As corrosion proceeds, an island-like rust layer is formed (Rust (1st) in Fig. 12). However, hydrogen entry is barely enhanced owing to the high potential and the pH at least of 4.0 during the 1st stage.

As the droplet spreads, the contact area between the Fe surface and the droplet increases, resulting in the spread of the ORR site and the thinning of the droplet. Thus, the ORR and corrosion are rapidly accelerated (2nd stage), and the rust layer grows further (Rust (2nd) in Fig. 12). In the outer region of the rust layer, corrosion is believed to proceed intensively because of the short distance to the ORR site, which increases the concentration of Fe^{2+}. In addition, rust precipitation is accelerated adjacent to the ORR site owing to alkalisation. Furthermore, dissolved O_2 is readily supplied under the thin droplet and facilitates the oxidation reaction of Fe^{2+}. As a result, the rust layer tends to be thick in the outer region. Under the rust layer, the pH decreases to below 3.0 owing to the hydrolysis reactions of Fe ions [5,6].

$$4Fe^{2+} + O_2 + 6H_2O \rightarrow 4FeOOH + 8H^+ \quad (7)$$

Moreover, the potential of the corroded area becomes lower than the electrode potential of the HER.

$$2H^+ + 2e^- \rightarrow H_2 \quad (8)$$

Thus, the HER occurs on the corroded area. Owing to the decrease in the potential and pH, the coverage of adsorbed hydrogen is increased, promoting the hydrogen absorption reaction (hydrogen entry) on the corroded area.

$$H^+ + e^- \rightarrow H_{ad} \quad (9)$$

$$H_{ad} \rightarrow H_{ab} \quad (10)$$

As the NaCl droplet is dried, the concentration of chloride ions drastically increases and the solution pH decreases owing to the decrease in the volume of the NaCl droplet, thus further promoting Fe dissolution, acidification, and hydrogen entry. Because the electrode potential of the HER increases with a decrease in pH, the potential of the HER sites (corroded area) increases with acidification. In conclusion, a decrease in pH is a critical factor facilitating hydrogen entry on the corroded area where the potential is lower than the electrode potential of the HER. Because the pH under the rust layer was not measured in this study, further investigation is required to determine the accurate pH value that triggers the enhancement of hydrogen entry.

After the disappearance of the droplet, hydrogen entry becomes moderate or almost ceased. The rust layer contains the NaCl solution

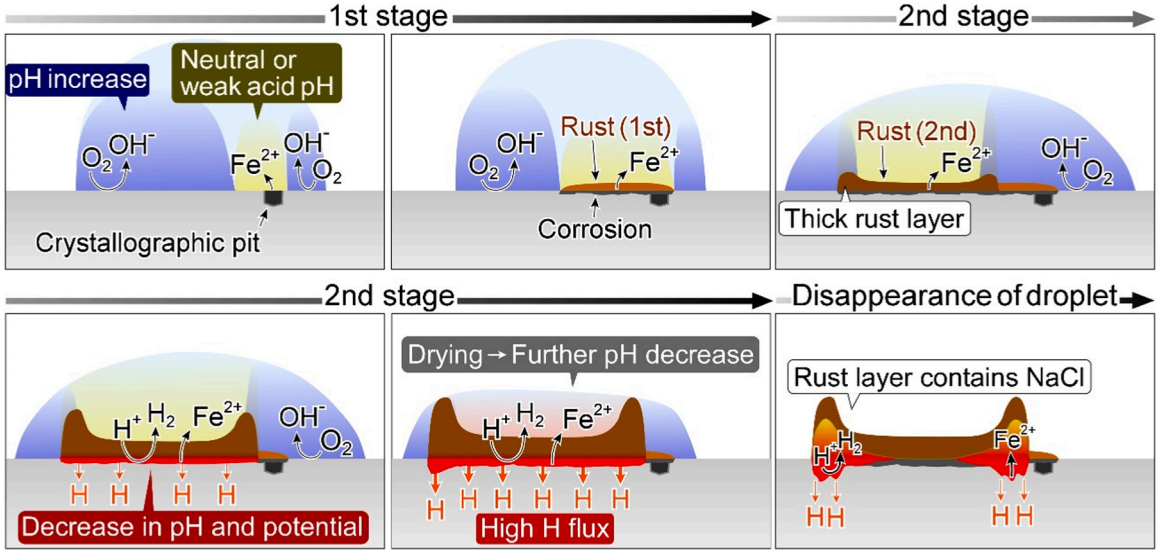

Fig. 12. Mechanism of hydrogen entry into an Fe sheet under a NaCl droplet.

immediately after the disappearance of the droplet, and the amount of the NaCl solution contained depends on the thickness of the rust layer. Therefore, corrosion and hydrogen entry proceed continuously under the thick rust layer for a long time in ambient air. Because the rust layer tends to be thick on the outer region, severe corrosion was caused by the concentrated NaCl solution, enhancing the hydrogen entry under the outer region in the rust layer even after the disappearance of the droplet.

4. Conclusions

A PANI-based hydrogenochromic sensor and thymol blue were used for the simultaneous visualisation of the hydrogen entry and pH distribution in a NaCl droplet, and the relationships between pH, hydrogen entry and rust precipitation were analysed. The effects of the solution pH on the corrosion morphology and corrosion-induced hydrogen entry were elucidated via electrochemical hydrogen permeation tests. The conclusions of this study are as follows.

- Hydrogen entry was barely enhanced by the initiation of large crystallographic pits, which formed during the initial stage of corrosion under the NaCl droplet, because crystallographic pitting proceeded in a weakly acidic NaCl solution at potentials higher than the electrode potential of the HER.
- Hydrogen entry was promoted under the island-like rust layer as general corrosion proceeded when the solution pH was below 3.0 and the potential of the corroded area was lower than the electrode potential of the HER.
- The hydrogen permeation current was not detected at pH 4.0, in both 0.1 M and 1 M NaCl. In 0.1 M NaCl, the OCP was –0.2 V vs. Ag/AgCl (3.33 M KCl) at pH 4.0, while it decreased to –0.65 V at pH 3.0, triggering the enhancement of hydrogen entry. The hydrogen permeation current at pH 2.0 was larger than that at pH 3.0, suggesting that the decrease in pH resulted in more severe corrosion and accelerated hydrogen entry.
- The pH decrease mainly contributed to the acceleration of hydrogen entry on the corroded area of the Fe surface where the potential was lower than the electrode potential of the HER.
- Hydrogen entry was not promoted in the non-corroded area where the solution pH was high owing to the ORR.
- The rust layer was thicker in the outer regions than in the centre of the rust-formed area because severe corrosion and alkalisation occurred near the ORR sites, and dissolved O_2 was readily supplied under the thin droplet, promoting the generation of oxyhydroxide and hydroxide of Fe ions.
- The thick rust layer contained a large amount of the concentrated NaCl solution, which continuously promoted corrosion and hydrogen entry for a long time, even after the disappearance of the droplet. Consequently, the amount of hydrogen that entered the Fe sheet under the thick rust layer was greater than that under the thin rust layer.

CRediT authorship contribution statement

Hiroshi Kakinuma: Project administration, Funding acquisition, Conceptualization, Methodology, Investigation, Data curation, Writing - original draft. **Sachiko Hiromoto:** Investigation, Writing - review & editing. **Tomohiko Hojo:** Investigation, Writing - review & editing. **Saya Ajito:** Writing - review & editing. **Motomichi Koyama:** Writing - review & editing. **Eiji Akiyama:** Supervision, Writing - review & editing.

Declaration of Competing Interest

The authors declare that they have no known competing financial interests or personal relationships that could have influenced the work reported in this paper.

Data availability

The authors do not have permission to share data.

Acknowledgement

This work was supported by JSPS KAKENHI Grants-in-Aid for Early-Career Scientists (JP23K13570).

Appendix A. Supporting information

Supplementary data associated with this article can be found in the online version at doi:10.1016/j.corsci.2024.112043.

References

[1] D. Hardie, E.A. Charles, A.H. Lopez, Hydrogen embrittlement of high strength pipeline steels, Corros. Sci. 48 (2006) 4378–4385, https://doi.org/10.1016/j.corsci.2006.02.011.
[2] I.M. Robertson, P. Sofronis, A. Nagao, M.L. Martin, S. Wang, D.W. Gross, K. E. Nygren, Hydrogen embrittlement understood, Metall. Mater. Trans. A Phys. Metall. Mater. Sci. 46A (2015) 2323–2341, https://doi.org/10.1007/s11661-015-2836-1.
[3] M.Y. Maeda, M. Koyama, H. Nishimura, O.M. Cintho, E. Akiyama, Pre-straining alters hydrogen-assisted cracking site and local hydrogen diffusivity in a nitrogen-doped duplex steel, Scr. Mater. 207 (2022) 114272, https://doi.org/10.1016/j.scriptamat.2021.114272.
[4] T. Hojo, E. Akiyama, H. Saitoh, A. Shiro, R. Yasuda, T. Shobu, J. Kinugasa, F. Yuse, Effects of residual stress and plastic strain on hydrogen embrittlement of a stretch-formed TRIP-aided martensitic steel sheet, Corros. Sci. 177 (2020) 108957, https://doi.org/10.1016/j.corsci.2020.108957.
[5] T. Tsuru, Y. Huang, M.R. Ali, A. Nishikata, Hydrogen entry into steel during atmospheric corrosion process, Corros. Sci. 47 (2005) 2431–2440, https://doi.org/10.1016/j.corsci.2004.10.006.
[6] T. Kushida, Hydrogen entry into steel by atmospheric corrosion, ISIJ Int 43 (2003) 470–474, https://doi.org/10.2355/isijinternational.43.470.
[7] S. Li, E. Akiyama, T. Shinohara, K. Matsuoka, W. Oshikawa, Hydrogen entry behavior into iron and steels under atmospheric corrosion, ISIJ Int 99 (2013) 651–658, https://doi.org/10.2355/tetsutohagane.99.651.
[8] S. Ajito, E. Tada, A. Ooi, A. Nishikata, Simultaneous measurements of corrosion potential and hydrogen permeation current of iron in an aqueous NaCl droplet, ISIJ Int 59 (2019) 1659–1666, https://doi.org/10.2355/isijinternational.ISIJINT-2020-583.
[9] A. Nazarov, F. Vucko, D. Thierry, Scanning Kelvin Probe for detection of the hydrogen induced by atmospheric corrosion of ultra-high strength steel, Electrochim. Acta 216 (2016) 130–139, https://doi.org/10.1016/j.electacta.2016.08.122.
[10] I. Flis-Kabulska, J. Flis, T. Zakroczymski, Enhanced hydrogen entry into iron from 0.1 M NaOH at definite potentials, Electrochim. Acta 53 (2008) 3094–3101, https://doi.org/10.1016/j.electacta.2007.11.041.
[11] E. Akiyama, S. Li, T. Shinohara, Z. Zhang, K. Tsuzaki, Hydrogen entry into Fe and high strength steels under simulated atmospheric corrosion, Electrochim. Acta 56 (2011) 1799–1805, https://doi.org/10.1016/j.electacta.2010.09.043.
[12] D. Rudomilova, T. Prošek, M. Ström, Hydrogen Entry into Steel Under Corrosion Products, Corrosion 77 (2021) 427–432, https://doi.org/10.5006/3675.
[13] M.A.V. Devanathan, Z. Stachurski, W. Beck, A Technique for the evaluation of hydrogen embrittlement characteristics of electroplating baths, J. Electrochem. Soc. 110 (1963) 886, https://doi.org/10.1149/1.2425894.
[14] S. Ajito, E. Tada, A. Ooi, A. Nishikata, Simultaneous measurements of polarization resistance and hydrogen permeation current of iron in an aqueous NaCl droplet, ISIJ Int 61 (2021) 1222–1228, https://doi.org/10.2355/isijinternational.ISIJINT-2020-583.
[15] S. Dey, A.K. Mandhyan, S.K. Sondhi, I. Chattoraj, Hydrogen entry into pipeline steel under freely corroding conditions in two corroding media, Corros. Sci. 48 (2006) 2676–2688, https://doi.org/10.1016/j.corsci.2005.10.003.
[16] Y. Sugawara, Y. Sakaizawa, A. Shibata, I. Muto, N. Hara, Detection of hydrogen distribution in pure iron using WO3 thin film, ISIJ Int 58 (2018) 1860–1867, https://doi.org/10.2355/isijinternational.ISIJINT-2018-236.
[17] S. Ajito, T. Hojo, M. Koyama, K. Fujita, E. Akiyama, Application of an iridium complex for detecting hydrogen permeation through pure iron, Int. J. Hydrog. Energy 45 (2020) 25580–25586, https://doi.org/10.1016/j.ijhydene.2020.06.113.
[18] H. Nishimura, S. Ajito, T. Hojo, M. Koyama, K.I. Fujita, Y. Shibayama, H. Kakinuma, E. Akiyama, Effect of Stretch-forming on Hydrogen Diffusion Behavior in High-strength Steel Sheet, Tetsu-To-Hagane/J. Iron Steel Inst. Jpn. 108 (2022) 316–324, https://doi.org/10.2355/TETSUTOHAGANE.TETSU-2021-096.
[19] H. Katayama, Visualization of hydrogen permeation behavior through steel materials by surface potential measurement, ISIJ Int 56 (2016) 478–482, https://doi.org/10.2355/isijinternational.ISIJINT-2015-314.
[20] H. Katayama, T. Katsumura, T. Akashi, Y. Tsutsumi, Hydrogen entry behavior on steel materials exposed to wet-dry cyclic corrosive environment using surface

potential measurement, ISIJ Int 61 (2021) 1215–1221, https://doi.org/10.2355/isijinternational.ISIJINT-2020-552.
[21] F. Vucko, V.S. Helbert, A. Nazarov, Quantification of Hydrogen Flux from Atmospheric Corrosion of Steel Using the Scanning Kelvin Probe Technique, Metals 13 (2023), https://doi.org/10.3390/met13081427.
[22] H. Kakinuma, S. Ajito, T. Hojo, M. Koyama, E. Akiyama, Real-time visualization of hydrogen distribution in metals using polyaniline: An ultrasensitive hydrogenochromic sensor, Adv. Mater. Interf. 9 (2022) 2101984.
[23] H. Kakinuma, S. Ajito, T. Hojo, M. Koyama, S. Hiromoto, E. Akiyama, In situ 2D mapping of hydrogen entry into an Fe sheet under a droplet of NaCl solution using a hydrogenochromic sensor, Int. J. Hydrog. Energy 47 (2022) 38468–38476, https://doi.org/10.1016/j.ijhydene.2022.09.006.
[24] H. Kakinuma, S. Ajito, T. Hojo, M. Koyama, S. Hiromoto, E. Akiyama, Simultaneous observations of the corrosion behavior of an Fe sheet and the associated hydrogen distribution therein employing a hydrogenochromic sensor, Corros. Sci. 206 (2022) 110534, https://doi.org/10.1016/j.corsci.2022.110534.
[25] S. Ajito, E. Tada, A. Ooi, A. Nishikata, Hydrogen Absorption Behavior of Pre-Rusted Steels under an NaCl Droplet, J. Electrochem. Soc. 166 (2019) C243–C249, https://doi.org/10.1149/2.0591910jes.
[26] L. Martin, C. Sébastien, A. Gabillon, Hue and saturation in the RGB color space, in: A. Elmoataz, O. Lezoray, F. Nouboud, D. Mammass (Eds.), Image Signal Process. 6th Int. Conf. ICISP 2014, Springer International Publishing, Cherbourg, France, 2014, pp. 203–212, https://doi.org/10.1007/978-3-319-07998-1_23.
[27] H. Kakinuma, S. Ajito, T. Hojo, M. Koyama, E. Akiyama, In situ visualization of misorientation-dependent hydrogen diffusion at grain boundaries of pure polycrystalline Ni using a hydrogen video imaging system, Acta Mater. 263 (2024) 119536 doi.org/10.1016/j.actamat.2023.119536.
[28] H. Kakinuma, S. Ajito, M. Koyama, E. Akiyama, Microscopic visualization of hydrogen diffusion in UNS S32750 super duplex stainless steel: Roles of crystal structure and grain size, Int. J. Hydrog. Energy 59 (2024) 866–873, https://doi.org/10.1016/j.ijhydene.2024.02.069.
[29] Y. Shi, E. Tada, A. Nishikata, A Method for Determining the Corrosion Rate of a Metal under a Thin Electrolyte Film, J. Electrochem. Soc. 162 (2015) C135–C139, https://doi.org/10.1149/2.0101504jes.
[30] M. Stratmann, H. Streckel, K.T. Kim, S. Crockett, On the atmospheric corrosion of metals which are covered with thin electrolyte layers - III. The measurement of polarization curves on metal surfaces which are covered by thin electrolyte layers, Corros. Sci. 30 (1990) 715–734.
[31] G.S. Frankel, M. Stratmann, M. Rohwerder, A. Michalik, B. Maier, J. Dora, M. Wicinski, Potential control under thin aqueous layers using a Kelvin Probe, Corros. Sci. 49 (2007) 2021–2036, https://doi.org/10.1016/j.corsci.2006.10.017.
[32] E. Akiyama, K. Matsukado, M. Wang, K. Tsuzaki, Evaluation of hydrogen entry into high strength steel under atmospheric corrosion, Corros. Sci. 52 (2010) 2758–2765, https://doi.org/10.1016/j.corsci.2009.11.046.
[33] E. Hudson-Heck, R.H. Byrne, Purification and characterization of thymol blue for spectrophotometric pH measurements in rivers, estuaries, and oceans, Anal. Chim. Acta 1090 (2019) 91–99, https://doi.org/10.1016/j.aca.2019.09.009.
[34] S. Li, L.H. Hihara, In situ Raman spectroscopic study of NaCl particle-induced marine atmospheric corrosion of carbon steel, J. Electrochem. Soc. 159 (2012) C147–C154.
[35] T. Nishimura, H. Katayama, K. Noda, T. Kodama, Electrochemical behavior of rust formed on carbon steel in a wet/dry environment containing chloride ions, Corrosion 56 (2000) 935–941.
[36] N.D. Tomashov, Development of the electrochemical theory of metallic corrosion, Corrosion 20 (1964), 7t-14t.